CHEMICAL PHYSICS

Microwave-assisted, performance-advantaged electrification of propane dehydrogenation

Yeonsu Kwak[1,2], Cong Wang[2], Chaitanya A. Kavale[3], Kewei Yu[1,2], Esun Selvam[1,2], Reyes Mallada[4], Jesus Santamaria[4], Ignacio Julian[5], Jose M. Catala-Civera[6], Himanshu Goyal[3], Weiqing Zheng[2], Dionisios G. Vlachos[1,2]*

Nonoxidative propane dehydrogenation (PDH) produces on-site propylene for value-added chemicals. While commercial, its modest selectivity and catalyst deactivation hamper the process efficiency and limit operation to lower temperatures. We demonstrate PDH in a microwave (MW)–heated reactor over $PtSn/SiO_2$ catalyst pellets loaded in a SiC monolith acting as MW susceptor and a heat distributor while ensuring comparable conditions with conventional reactors. Time-on-stream experiments show active and stable operation at 500°C without hydrogen addition. Upon increasing temperature or feed partial pressure at high space velocity, catalysts under MWs show resistance in coking and sintering, high activity, and selectivity, starkly contrasting conventional reactors whose catalyst undergoes deactivation. Mechanistic differences in coke formation are exposed. Gas-solid temperature gradients are computationally investigated, and nanoscale temperature inhomogeneities are proposed to rationalize the different performances of the heating modes. The approach highlights the great potential of electrification of endothermic catalytic reactions.

INTRODUCTION

Global warming from greenhouse gas (GHG) emissions is driving the electrification of the transportation and power sectors using renewable energy (*1*). With these ongoing advances, the industrial sector will soon become the topmost polluting sector. The chemicals and refinery industries are the top contributors to GHG emissions (*2*), followed by the cement, steel, and food industries also important. Hydrogen and its associated derivatives (ammonia and methanol) and light olefins (ethylene and propylene) are the highest CO_2-emitting chemical processes (*3*). Their decarbonization is much more complex than the transportation and power sectors because of their inherent complexity and high integration. Unlike ammonia and methanol production, which are exothermic reactions, olefins' production is an endothermic process. It requires high temperatures (>500°C) and energy fluxes. These endothermic reactions are at the core of the industrial high-temperature process heat sector (*4*). The high temperatures challenge traditional electrocatalysis as a means of electrification.

Propylene is a platform molecule in the petrochemical industry for many value-added chemicals (*5*, *6*). Its demand keeps increasing, while its production has not kept up (known as the propylene gap). Propylene has historically been made via energy- and carbon-intensive processes, specifically naphtha steam cracking and fluid catalytic cracking. Over the last decade, the United States has been leveraging shale gas abundance (and low cost) through the nonoxidative propane dehydrogenation (PDH) (*7*). Universal Oil Products implemented the Oleflex process using $PtSn/Al_2O_3$ and Lummus Technology the Catofin process using Cr_2O_3/Al_2O_3 (*8*). The latter catalyst suffers from toxicity. PDH is an equilibrium-limited reaction and is favored at high temperatures. The rapid coke deposition requires frequent catalyst regeneration, making the process complex and less productive. The thermal shock during oxidative regeneration can lead to catalyst sintering (*9*). Hydrogen is often cofed with propane to suppress catalyst deactivation by decreasing the coke precursor and facilitating propylene desorption (*10*). However, hydrogen use incurs additional costs and shifts the equilibrium to the reactant side. Given the carbon intensity of H_2 production, it is desirable to eliminate it. Given the above technical barriers, improving the PDH technology can be impactful. The high risk of emerging technologies and the multibillion-dollar investment needed for large-scale manufacturing create substantial obstacles to the penetration of these technologies.

Emerging process electrification (PE) technologies, such as Joule heating, plasma, and microwaves (MWs), are essential to achieve zero emissions (*11*, *12*), but these processes are neither commercial nor well understood. While ideal for modular skids, exploiting co-benefits stemming from PE can enhance their economic viability, given the higher cost of electricity and modules compared to large-scale equipment. For example, MW-assisted heating of susceptible media (with a high loss tangent, tan δ) can bypass heat transfer limitations (wall resistance and slow heat transfer from the wall to the center of a reactor tube) of conventional heating (CH) furnaces. By heating a reactor rapidly and volumetrically (*13*), one can enable modular manufacturing with an efficiency of >90% (*14*) (versus furnaces of typically <47%) and, thus, halve the energy use. However, MW application to high-temperature chemistries (>500°C) has been limited, as the electromagnetic field focuses on touching points of catalyst pellets (*15*), potentially causing arcing and thermal runaway.

In this work, we introduce the MW reactor, explore the cobenefits of PE of PDH under MWs over $PtSn/SiO_2$ catalyst and compare

[1]Department of Chemical and Biomolecular Engineering, University of Delaware, 150 Academy St., Newark, DE 19716, USA. [2]RAPID Manufacturing Institute, Catalysis Center for Energy Innovation and Delaware Energy Institute, 221 Academy St., Newark, DE 19716, USA. [3]Department of Chemical Engineering, Indian Institute of Technology (IIT) Madras, Chennai, Tamil Nadu 600036, India. [4]Instituto de Nanociencia y Materiales de Aragón (INMA), Consejo Superior de Investigaciones Científicas (CSIC-Universidad de Zaragoza), Zaragoza 50018, Spain. [5]CIRCE Foundation, Zaragoza 50018, Spain. [6]ITACA Institute, Universitat Politècnica de València, Valencia 46022, Spain.
*Corresponding author. Email: vlachos@udel.edu

its performance with CH. We demonstrate minimal coke formation by suppressing the gas-phase chemistry, a different coke formation mechanism, slower sintering, and improved activity, durability, and selectivity under MWs. These cobenefits are essential for minimizing downstream separation costs and excess energy use.

RESULTS

We use a SiC monolith filled with $PtSn/SiO_2$ catalyst and quartz pellets (Fig. 1A) (*16*) in the micro-fixed bed reactor, which affords a catalyst loading nearly as high as conventional fixed beds to ensure high productivity and compact devices. SiC's outstanding MW-absorbing properties enable excellent coupling with the electromagnetic field (*17*). We have chosen SiC compared to other MW absorbing materials, such as iron oxide, as previous calculations (*18*) indicate that its high thermal conductivity is ideal for spreading the energy and avoiding arcing and macroscopic temperature gradients. An isothermal furnace is used for CH experiments with temperatures measured by a thermocouple (TC) (Fig. 1B). Digital and infrared (IR) images of the reactor wall visually confirm temperature uniformity of the MW-heating region (thermal window = 15 mm; Fig. 1C). The temperature measured at the center using a fiber Bragg grating (FBG) in high-temperature processes and at the wall using a high-temperature IR (HT-IR) camera was 700°C (± 5°C) and 660°C (± 2°C), with a ~6% deviation (Fig. 1D). The temperature field under MWs exhibits modest radial inhomogeneity as the edges lose heat, resulting in higher center temperatures (T_{center}); this is known as the inverse temperature profile.

COMSOL Multiphysics simulations (*19*, *20*) predict the three-dimensional (3D) temperatures and power consumption of MWs. The predicted power consumption is within 5% of the experimental values at comparable temperatures (Fig. 1E), demonstrating the accuracy of the model. Inset images in Fig. 1E show the model cross-section 2D temperatures of MW500 and MW700. Figure 1 (F and G) shows the corresponding radial and axial temperature distribution, respectively. The highest temperature is at the center, emphasizing the importance of accurate bulk measurements until now lacking (*21*). The temperature increases rapidly within <5 mm from the monolith entrance due to conduction and radiation and remains nearly uniform within the bed. The gas and solid phase within the monolith channels quickly reach thermal equilibrium (*18*). At the given flow rate, the hot gas cools down to room temperature within ~10 mm upon exiting the monolith. Overall, the computations indicate that the catalytic bed temperatures under MW radiation are uniform in the longitudinal direction and expose small gradients near the walls directly exposed to static air. We hypothesize that the cold upstream gas and the rapid cooling of the

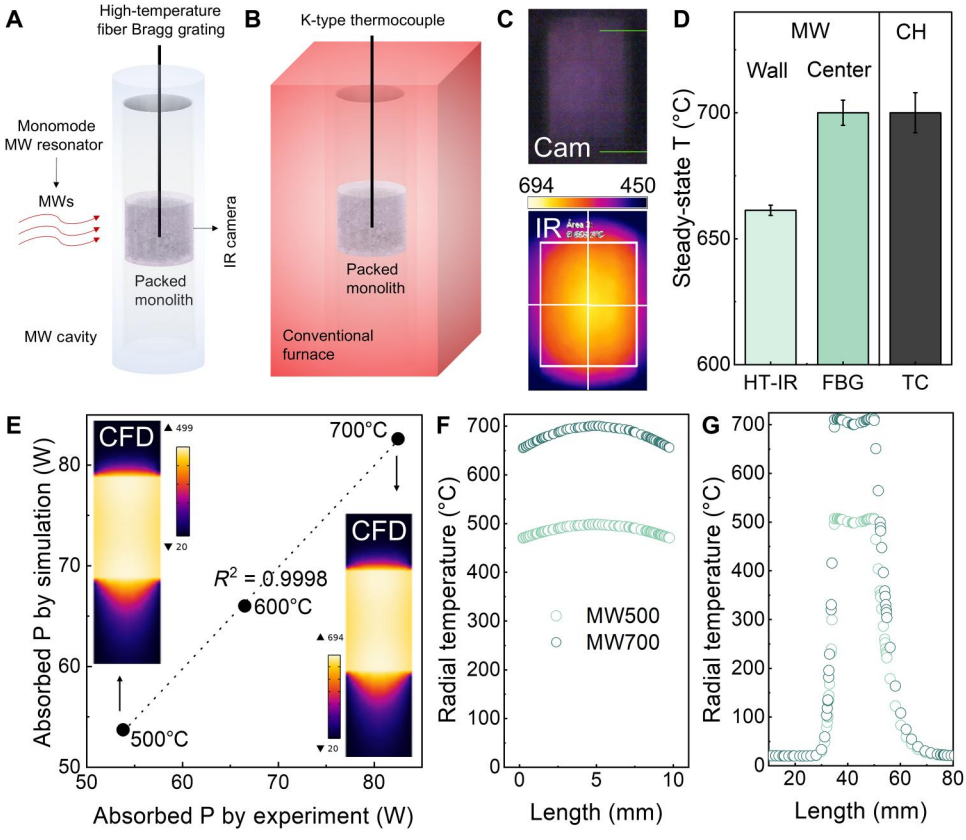

Fig. 1. High-temperature PDH reactor heating and temperature fields. (**A**) MW-assisted and (**B**) CH. (**C**) Thermal imaging of the MW reactor at 700°C by digital and IR cameras. (**D**) Experimentally measured center (probe) and wall (HT-IR, high-temperature IR camera) temperatures for MWs (FBG) and CH (TC); error bars refer to temperature fluctuation over time-on-stream (TOS). Computational insights over local temperature distribution under MWs. (**E**) Parity plot of the absorbed MW power estimated by experiment and COMSOL simulation at 500°, 600°, and 700°C of T_{center}. (5% C_3H_8 in He, flow rate = 50 SCCM; inset: Computational fluid dynamics (CFD)-predicted temperatures under MWs). (**F**) Simulation-predicted radial and (**G**) axial temperature distribution over the cross section under MWs.

outlet gas flow under MWs minimize undesirable side reactions of PDH before and after the MW region that can dominate a laboratory microreactor in a furnace where the entire quartz tube is exposed to high temperatures (*22*). To assess this hypothesis, we compare the performance of the two processes at increasing temperatures (denoted as MW*x* and CH*x*, where *x* is the temperature in °C).

The MW and CH reactor performances were identical at 500°C and low weight hourly space velocity (WHSV) of 2.95 g_{C3H8} g_{cat}^{-1} $hour^{-1}$, when the reaction rates are relatively low (Fig. 2A). The comparable reaction rates are an indirect manifestation of the same temperature, as the conversion (near) equilibrium is dictated by pressure and temperature only. The data corroborate with Fig. 1, as the conversion under MWs and CH reactors is close to the thermodynamic equilibrium conversion at this temperature (fig. S1). At 500°C and faster flows, without hydrogen in the feed, the time-on-stream (TOS) performance of MWs and CH differ; the PDH rate is higher under MWs, especially at long TOS (Fig. 2B). The propylene selectivity is high in both heating modes due to the excellent performance of the PtSn catalyst (>99.9%). The cracking of propane to methane and C_2 hydrocarbons is slow at this temperature. Active site densities were assessed using post-catalytic ethylene hydrogenation at low temperatures (Fig. 2C), a probe reaction to estimate the remaining Pt-based active sites (*23*). The MW500 sample retains most of its active sites but loses most of its EtH activity within 1 min in CH. This difference could be attributed to a small proportion of Pt nanoparticles in the fresh sample, verified by x-ray diffraction (XRD) (fig. S2), which shows higher initial activity for ethane (EtH) than PtSn. PtSn, with an atomic ratio of 1:1, exhibits nearly 10 times lower turnover frequency than Pt in EtH (*24*). These Pt nanoparticles are prone to rapid deactivation under CH, leaving only PtSn as the active component that also experiences gradual deactivation. In contrast, Pt deactivation may be delayed when MWs are used (vide infra).

To further capture the change in active site densities of Pt and PtSn, we used diffuse reflectance infrared Fourier transform spectroscopy (DRIFTS) using CO as a probe (fig. S3). The fresh Pt/SiO_2 has typical CO adsorption on nanoparticles, with the shoulder peak at ~2070 cm^{-1} assigned to terrace sites and the peaks lower than 2060 cm^{-1} to step sites. The addition of Sn red-shifts the CO stretch band, in line with the literature (*25*). Pt deactivates very fast in PDH due to coke [fig. S3A and (*9*, *26*)]. The CO peak area decreases much more slowly on the $PtSn/SiO_2$ sample, likely due to Sn that enhances the desorption of propylene whose further chemistry leads to coke (*27*). Nevertheless, the $PtSn/SiO_2$ catalyst still experiences deactivation under CH500 conditions. The relationship between the relative activity of CH500 at 29.5 g_{C3H8} g_{cat}^{-1} $hour^{-1}$ and the CO peak area (inset of fig. S3B) suggests that the deactivation may be attributed to the loss of PtSn active sites. The space-time yield (STY) of propylene after 3-hour TOS under CH and MWs depicts the overall performance (intrinsic activity and stability) of our and literature CH PtSn catalysts [table S1 and (*28*–*44*)]. Some literature introduced advanced synthesis with PtSn catalysts compared to our conventional incipient wetness impregnation-based synthesis, and most studies cofeed H_2 to alleviate coke formation, extend catalyst lifetime, and increase the reaction rate. Despite differences, key points are still evident. Figure 3A displays the PDH rate versus WHSV. The increase of the WHSV generally leads to an increase in reaction rates under external diffusion-limited conditions, and the rates become invariant under kinetic-limited conditions (*45*). The PDH rate–WHSV data of CH depict such a performance within a narrow temperature range at low WHSV (the gray dotted line is an eye guide indicating an upper bound). Our CH data lie below the line due to unfavorable operating conditions and the use of conventional catalysts that deactivate. Notably, MWs achieve a STY of 9.9 g_{C3H6} g_{cat}^{-1} $hour^{-1}$ at 600°C and 29.5 g_{C3H8} g_{cat}^{-1} $hour^{-1}$ without H_2 addition and surpass CH at fast flows.

In literature, very few studies report data without H_2 in the feed due to rapid coking. The influence of the H_2/C_3H_8 entrance ratio and temperature on STY is summarized in Fig. 3B. Higher temperatures improve the CH activity, especially when considerable fractions of H_2 are used. A molecular ratio of $H_2/C_3H_8 > 1$ can lead to a higher STY (*10*). The higher STY with H_2 present that pushes the reverse reaction indicates that the catalyst deactivation is crucial under CH. Low STYs are observed, even with H_2 cofeed, for less performing catalysts, e.g., compare bubble sizes of (*37*) at the top right. MW500 displays a moderate yield even without feeding

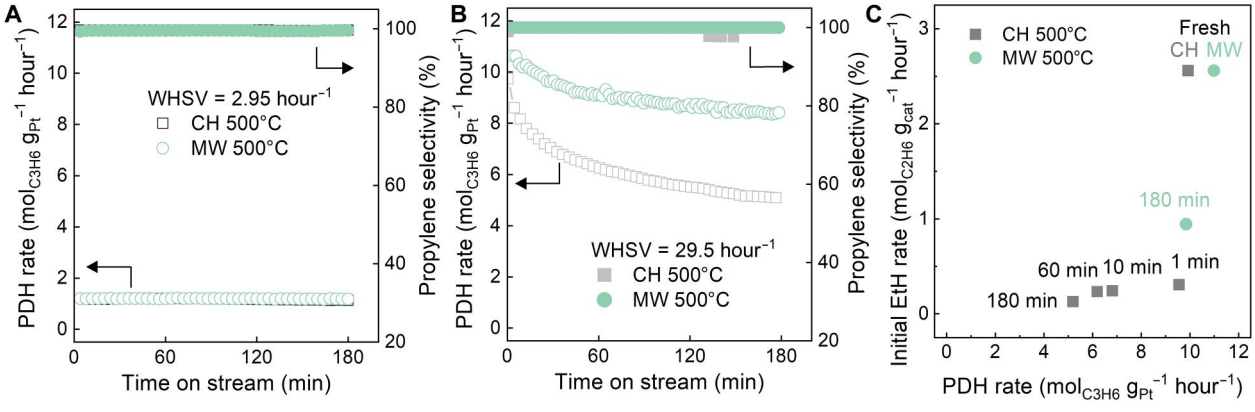

Fig. 2. PDH performances under CH and MWs. Propylene formation rates (left, *y* axis) and selectivity (right, *y* axis) at (**A**) 500°C and 2.95 g_{C3H8} g_{cat}^{-1} $hour^{-1}$, (**B**) 500°C and 29.5 g_{C3H8} g_{cat}^{-1} $hour^{-1}$. (**C**) Initial ethylene hydrogenation (EtH) rates for fresh and post-catalysis samples, run for times indicated, at 45°C, 17.0 g_{C2H4} g_{cat}^{-1} $hour^{-1}$, and $H_2/C_2H_4 = 3.26$ versus the PDH rate at 500°C and 29.5 g_{C3H8} g_{cat}^{-1} $hour^{-1}$. Fresh PDH rates ($r_{C3H6,0}$) are extrapolated to $t = 0$ min. For PDH experiments, $C_3H_8 = 5\%$ in He balance and H_2 cofed = 0.

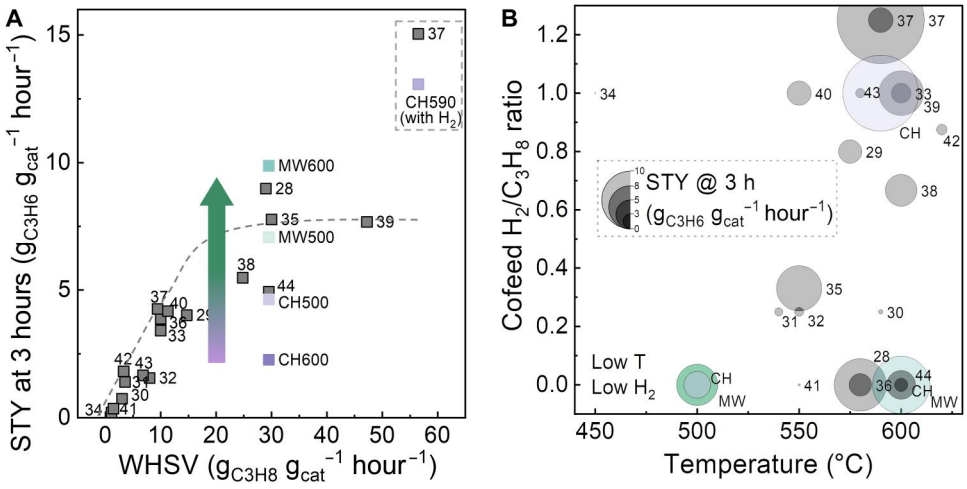

Fig. 3. PtSn performance comparison. (**A**) STY (g_{C3H6} g_{cat}^{-1} $hour^{-1}$) after 3-hour TOS versus WHSV. The dotted box compares the highest yield in literature CH experiments and our PtSn/SiO_2 catalyst. The gray line guides the eye. (**B**) STY (bubble size) after 3 hours at various operating conditions (cofeed H_2 to C_3H_8 ratio versus temperature). The larger the bubble, the larger the STY. The numbers in both panels indicate references, summarized in table S1.

hydrogen, superior to many state-of-the-art PtSn catalysts that exhibit good activity and stability only with cofed hydrogen. We believe the local heating effect under MWs retards deactivation and affords higher temperatures without external hydrogen. Extensive characterizations of the spent catalyst will be discussed next.

High-resolution transmission electron microscopy (TEM) images of fresh, reduced PtSn nanoparticles have bare nanoparticles (Fig. 4A and fig. S4) with a standard lognormal distribution of an average diameter of ~3.0 nm. After the reaction, the CH500-3h catalyst exhibits modest agglomeration (Fig. 4B and fig. S5), with small and larger than 6-nm particles coexisting. Our data are consistent with a previous report observing sintering from 3.8 to 5.3 nm at 500°C for 24-hour reaction (*46*). Frequently observed overlayers indicate amorphous carbon [>0.4 nm; (*47*)] or SnO_2 segregation on the catalyst that reduces activity, consistent with the active site loss in EtH probe reaction (Fig. 2C). Because XRD suggests no phase separation of the active metals in both processes (fig. S2), the overlayer is mostly likely carbonaceous deposits. The growth of particle size under CH suggests that Ostwald ripening may be accelerated by the coke precursors, causing catalyst particle sintering (*48*). Under MWs, the particle growth is highly suppressed and overlayers are less frequently seen (Fig. 4C and fig. S6). Although heat conduction is fast over scales longer than micrometers, the heat transfer is dominated by phonons rather than Fourier′s law and may rationalize local temperature gradients between the active sites and the support (*49*).

We use O_2 temperature-programmed oxidation (TPO) to provide insights into the hardness, amount, and location of coke (*50*). The coke is much less in MW500-3h than in CH500-3h [0.37 weight % (wt %) versus 1.55 wt %, respectively; Fig. 4D; calculation in note S1], consistent with the results above. The main peaks at 360°C for MWs and CH are attributed to coke adjacent to the active metal sites that oxidize it easier (*26*). For the MW500-3h, the sporadic small shoulder peaks at high temperatures may suggest coke on the support. The CH and MW coke is carbon-rich with no prominent hydrogen appearing as H_2O and no CO forming (fig. S7), as reported in other works (*51*), consistent with the lack of hydrogen (*52*). Ex situ Raman shows defective and graphitic features of carbon under CH and MW (Fig. 4E) (*53*). CH500-30min and MW500-3h show mild fluorescent interference, indicative of relatively immature carbon (*54*), consistent with TPO that MWs delay coke formation. The deconvolution of CH500-3h and MW500-3h Raman data (fig. S8) shows that the MW500-3h sample has a higher I_{D3}/I_G and I_{D4}/I_G ratio, i.e., the deposited coke under MWs is more amorphous or contains disordered graphitic lattice (*55*). The less graphitized coke precursor may be easily removed from the active sites and absorb MWs, giving defective features (*56*).

Experiments conducted at 700°C with a high WHSV of 29.5 g_{C3H8} g_{cat}^{-1} $hour^{-1}$ demonstrate distinct initial PDH rates under MWs and CH (Fig. 5A). Under CH, the initial C_3H_8 conversion rate to C_3H_6 was not measurable due to rapid deactivation. The propylene rate is lower than that of propane, indicating selectivity loss; thermal cracking to methane and C_2 hydrocarbons occurs. By carrying experiments without a catalyst [fig. S9 and (*57*)], the catalyst′s contribution to propylene formation was estimated by subtracting the rate from the total (Fig. 5B and note S1). Gas-phase chemistry dominates in CH at high temperatures, as the entire volume of the microreactor in the furnace carries the reaction.

The catalyst undergoes sintering with carbonaceous layers onto the particles and no prominent support-deposited carbon under CH (Fig. 5C), different from one under MWs (Fig. 5D). No phase segregation occurred in XRD (fig. S10). The coke formed at short times oxidizes at low temperatures, suggesting less graphitized carbon forming rapidly upon exposure to propane (Fig. 5E). After 3 hours, amorphous layers on top of Pt (360°C) and SiO_2 (560°C) and carbon fiber–like structures (>600°C) form away from the catalyst surface. Raman spectra exhibit a strong fluorescence with disparate curve features regardless of the light source or laser line (Fig. 5F). This feature observed in exhaust soot (*58*) or heavy residue (*59*) implies conjugated rings formed by polymerization of coke precursors. The fluorescence may also indicate immature carbon specimens and amorphous carbonaceous matter (*60*). Although the coke has a lot of defects (D_{total}/G = 3.13), its large

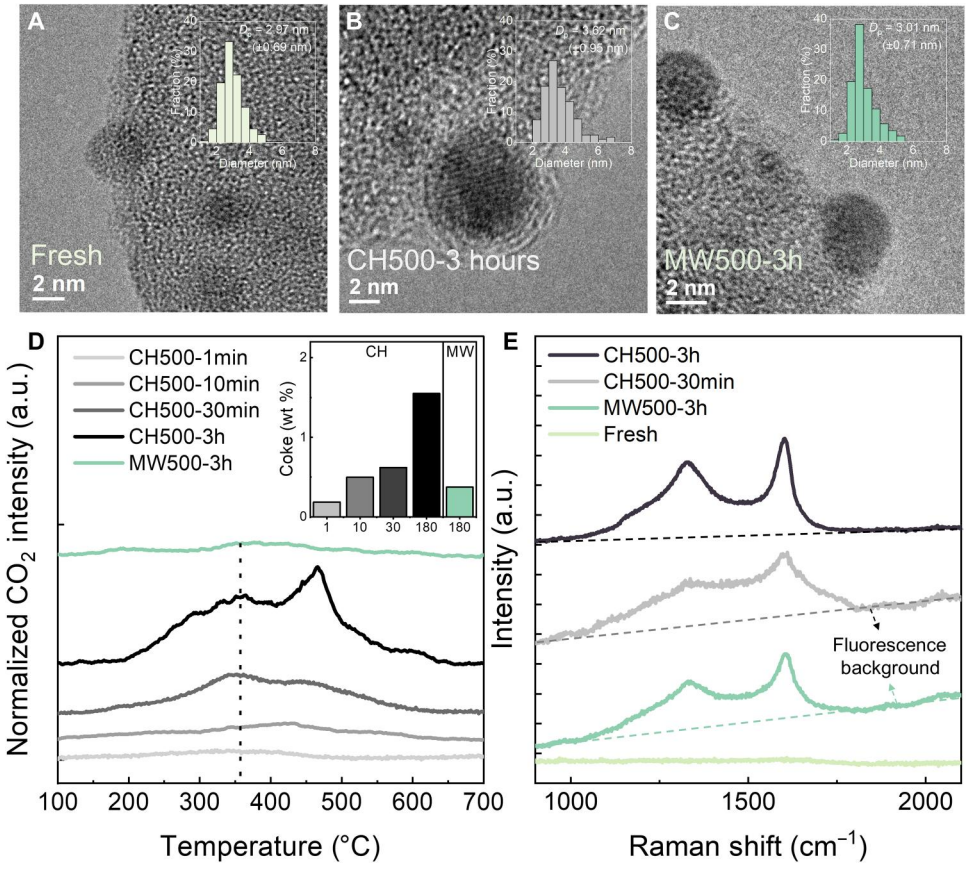

Fig. 4. Characterization of fresh and spent PtSn/SiO_2 catalysts. TEM images of (**A**) fresh, (**B**) CH, (**C**) MW samples (inset: particle size distribution). (**D**) CO_2 evolution spectra from O_2-TPO and (**E**) ex situ Raman spectra of fresh and spent catalysts at different TOS. The inset in (D) shows the carbon content for various TOS under CH and MWs. For PDH experiments, T_{center} = 500°C, WHSV = 29.5 g_{C3H8} g_{cat}^{-1} $hour^{-1}$, C_3H_8 = 5% in He balance, and H_2 cofed = 0. a.u., arbitrary unit.

amount blocks the PtSn active sites. Noncatalytic PDH using SiO_2 (Fig. 5G) shows that the gas-phase–derived carbon onto SiO_2 is low. Although gas-phase chemistry contributes less to direct carbon accumulation, the prominent Raman fluorescence (Fig. 5H) implicated gas-phase–derived carbon probably due to the cracked carbon products, e.g., ethylene, that contribute to the growth of coke.

MWs exhibit markedly different behavior. The selectivity to propylene (Fig. 5A) is high, and gas chemistry contributes slightly (Fig. 5B). The PtSn nanoparticles remain relatively intact (Fig. 5D and fig. S11). The data show that the loss of selectivity to propylene is due to unselective gas chemistry at high temperatures that lead to ethylene oligomerization to benzene, naphthalene, and other soot precursors driving enhanced coke formation in CH. MWs minimize gas-phase cracking due to localized heating, reducing deactivation, and maintaining high selectivity. We occasionally observe premature amorphous carbon on the support (a white dotted region in Fig. 5D). We postulate that MWs may facilitate the removal of coke precursors from the PtSn to the support, previously suggested as a prominent feature of Sn addition to Pt (*55*). Whether this removal entails surface diffusion or hydrogenation and desorption from the metal and redeposition on the support is unknown. We hypothesize that the coke precursors are highly MW absorbing and localize the electromagnetic field, creating nanoscopic temperature gradients that facilitate their removal. These nanoscopic gradients can persist due to the slower rate of energy dissipation at the nanometer scale (*61*). MWs generate less and different coke (Fig. 5E). The strong peak at ~560°C in O_2-TPO suggests carbon on the support that is oxidized and removed at elevated temperatures. It is likely that carbon build-up occurs gradually under MWs and mostly occurs on the support that does not obstruct the active sites.

Experiments with localized CH (LCH) were carried out to exploit the influence of gas-phase chemistry due to the furnace's large interior space (fig. S12). Both CH and LCH demonstrated similar performance at an internal temperature of 500°C, a temperature too low for gas-phase reactions to occur (fig. S13A), supported by similar TPO peaks and coke quantities (fig. S13B). At 700°C, the LCH reactor shows a lower apparent reaction rate, mainly because of the catalytic deactivation, despite the relatively mild gas-phase reactions (fig. S14A). This catalytic deactivation of LCH700 is similar to what is observed in the CH700 system. After 3 hours, the propylene production rate of LCH700 nearly matched the rate from the gas-phase reaction. TPO results indicate more coke in LCH700-3h than in CH700-3h and MW700-3h (fig. S14B). Merely reducing the gas-phase reaction volume was insufficient to match MWs. MWs not only solely reduce gas phase cracking but also influence microscopic temperature gradients between the active site and the support (*62*, *63*).

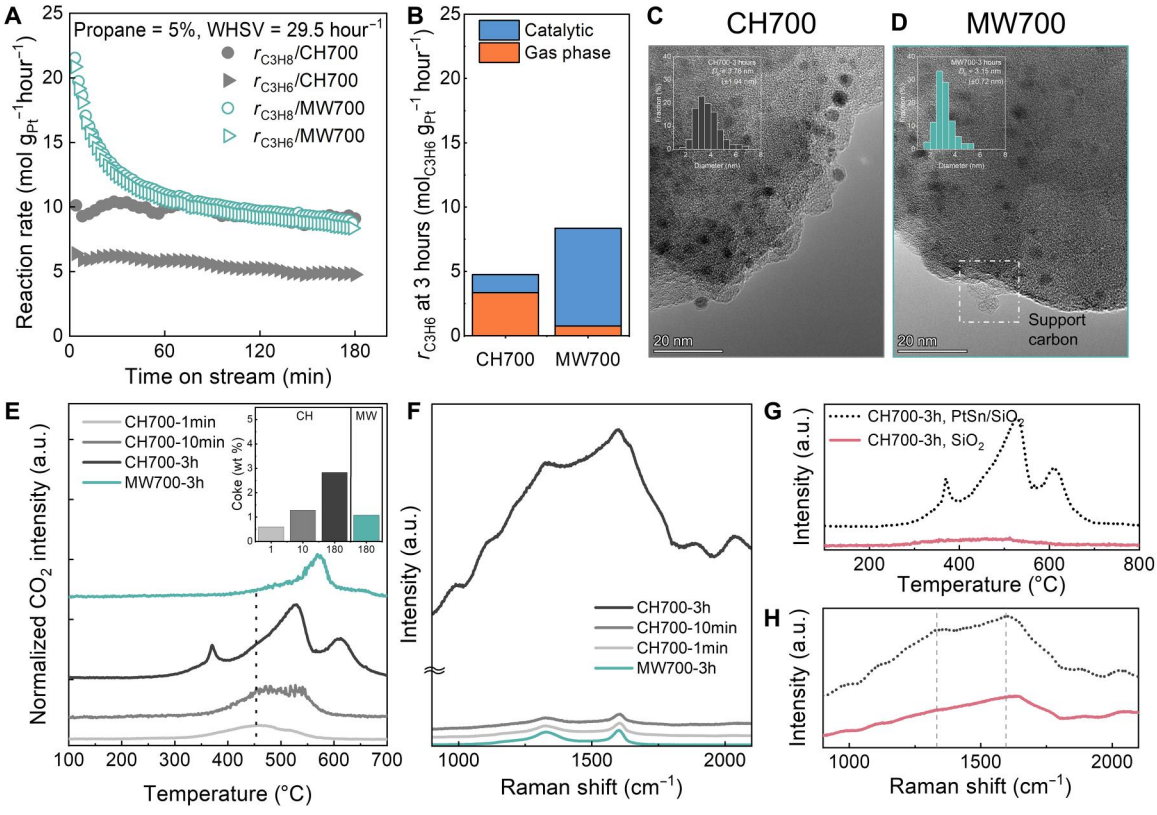

Fig. 5. PDH performance at high T_{center} under CH and MWs. (**A**) TOS data under CH and MWs for 3 hours (r_{C3H8} = propane consumption rate, r_{C3H6} = propylene production rate). (**B**) PDH rate after 3-hour TOS and catalyst and gas-phase contributions. TEM images of (**C**) CH700 and (**D**) MW700 (inset: particle size distributions). (**E**) CO_2 evolution spectra from O_2-TPO, (**F**) ex situ Raman spectra of CH and MW spent catalysts, (**G**) CO_2 evolution spectra from O_2-TPO, and (**H**) ex situ Raman spectra of CH700 spent catalyst and support. For PDH experiments, T_{center} = 700°C, WHSV = 29.5 g_{C3H8} g_{cat}^{-1} hour^{-1}, C_3H_8 = 5% in He balance, and H_2 cofed = 0.

To further elucidate the origin of deactivation, we exploited a higher partial pressure of propane (50% propane in He) at 700°C, maintaining high WHSV (29.5 g_{C3H8} g_{cat}^{-1} hour^{-1}). The MWs and CH PDH initial activities in Fig. 6A are similar, but the MW PDH shows enhanced selectivity and stability over time. The propylene selectivity of CH700 rapidly decreases from 80.4 to 40.8%, and that of MWs gradually decreases from 91 to 78%. The CH rate after 3-hour TOS approaches the noncatalytic one, indicative of complete catalyst deactivation. In contrast, the catalyst under MWs still has high activity (Fig. 6B). The CH700 sample suffers from sintering with no prominent support-deposited carbon (Fig. 6C). On the other hand, fibrous carbon is prevalent on MW700, and the PtSn nanoparticles remain intact (Fig. 6D and fig. S15). Fibrous coke on SiO_2 avoids blocking the active sites (*64*). In ethane aromatization under MWs, carbon nanotubes and fibrous coke formation have been reported (*65*, *66*) besides amorphous coke. We did not observe any carbon fiber–associated problems such as plugging and pressure drop in the MW reactor. Catalyst regeneration experiments indicate that catalysts exposed at 700°C have lower initial activity than 600°C catalysts, presumably due to minor sintering, but are more durable than catalysts exposed to CH (fig. S16).

MWs generate less coke, but the difference from CH is not as pronounced as at low propane partial pressures (Fig. 6E). Notably, the MW700 sample has a broad shoulder peak in the first derivative of the TGA curve (DTG) (inset of Fig. 6E) and O_2-TPO (Fig. 6F), which can be deconvoluted into two peaks, suggesting carbon on the support oxidized at elevated temperatures. Brunauer-Emmett-Teller analysis indicates that the MW700 sample loses a larger portion of the mesopores and surface area (fig. S17) than CH700, possibly because of the carbon on the support. However, as the MW coke deposits are not thick to block pores (*65*), the reactants still reach active sites leading to high stability. XRD analysis rules out alloy composition change (such as Pt_3Sn to PtSn) under both heating modes (fig. S18) and crystalline/bulk SnO_x formation. Ex situ Raman spectra of CH700 exhibit a strong fluorescence with disparate curve features (Fig. 6G and fig. S19), the same as low partial pressures. On the other hand, the MW700 catalyst shows less intense and clear carbon bands with a large *D* bands intensity.

X-ray photoelectron spectrometry (XPS) analysis is summarized in fig. S20. The Pt 4f spectra of MW700 and CH700 samples remain the same shape and position as the fresh PtSn catalyst. For Sn 3d, the MW700 sample exhibited predominantly centered peaks around 485.7 eV similar to the fresh sample indicating PtSn formation (*28*). However, a shoulder peak of Sn (0) around 485 eV notably appears in CH700, possibly indicating the segregation of Sn from PtSn that can be reduced more easily. Although both Pt 4f′s and Sn 3d′s intensities of the spent samples dropped noticeably, very likely due to the coke formation, the unchanged chemical

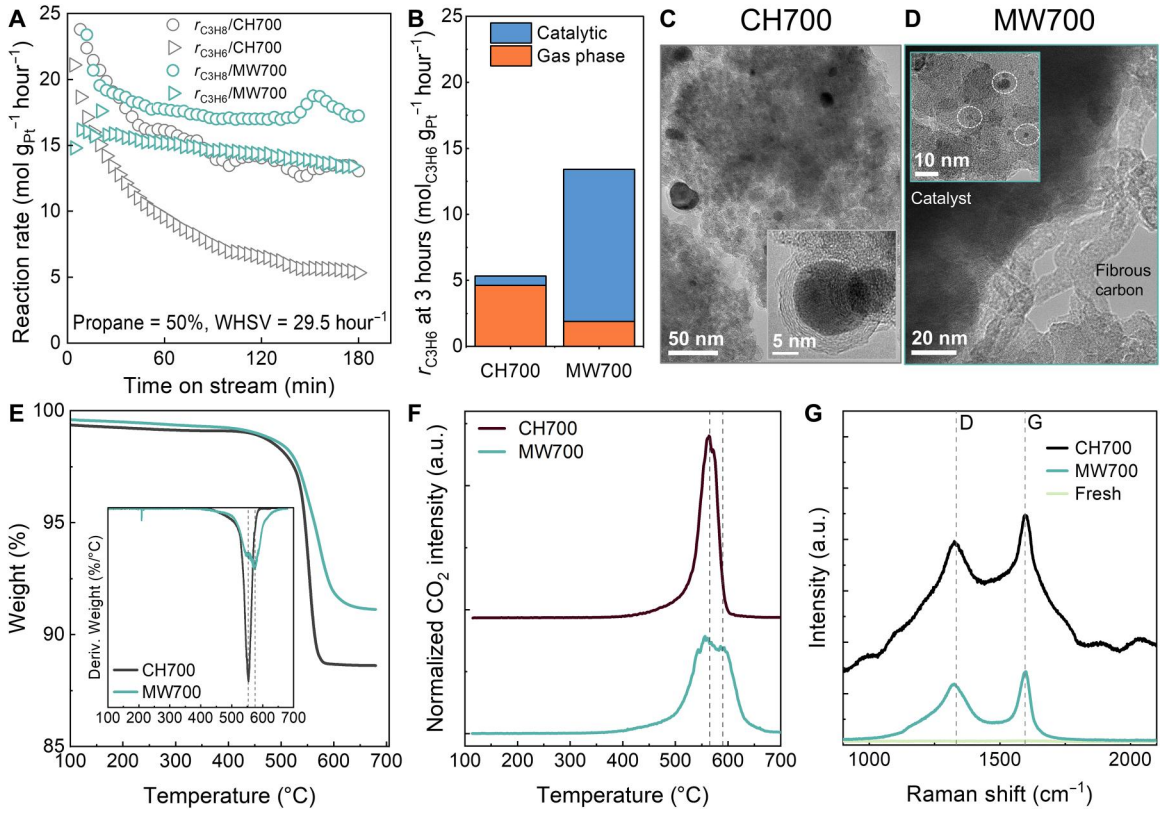

Fig. 6. PDH performance at extreme conditions of highly concentrated feed, high T_{center}, and high WHSV under CH and MWs. (**A**) TOS data under CH and MWs for 3 hours. (**B**) PDH rate after 3-hour TOS and catalyst and gas-phase contributions. TEM images of (**C**) CH700 (inset: coked and agglomerated nanoparticles) and (**D**) MW700 (inset: small PtSn nanoparticles). (**E**) Thermogravimetric analysis (TGA) and its first derivative curves (coke content = 8.5 and 10.8 wt % for MWs and CH), (**F**) CO_2 evolution spectra from O_2-TPO, and (**G**) ex situ Raman spectra of CH and MW spent catalysts. For PDH experiments, TOS = 3 hours, T_{center} = 700°C, WHSV = 29.5 g_{C3H8} g_{cat}^{-1} $hour^{-1}$, C_3H_8 = 50% in He balance, and H_2 cofed = 0.

environment of Pt and Sn in the MW700 sample indicates that MW PDH may inhibit Sn segregation from PtSn and retain high reactivity in PDH. C 1s spectra show more coke under the CH700 than MW700 (fig. S20C), as evidenced by C/(Pt + Sn) atomic ratios, consistent with O_2-TPO and thermogravimetric analysis (TGA).

An additional accelerated aging test at 800°C (fig. S21) indicated particle sintering in CH with a 4.77-nm average particle size and a large fraction being >8 nm (fig. S22) but small nanoparticles (3.65 nm) with a narrow distribution under MWs. MWs still maintain high selectivity to propylene and a good carbon balance at 800°C (fig. S23), but the STY at 800°C is low due to rapid deactivation as gas-phase chemistry is non-negligible. All findings (figs. S24 to S26) corroborate that MWs lead to support-relevant coke deposition with less active site agglomeration.

DISCUSSION

MWs offer an alternative route to CH toward chemical industry decarbonization using green electricity. They can supply process heat for making the most demanding—very high temperature and flux—chemicals volumetrically and rapidly and with higher energy efficiency, resulting in energy savings. Their widespread application in conventional fixed beds has been limited owing to arcing at contact points between particles (*63*) that lead to coke deposition, concentrating the electromagnetic field and leading eventually to thermal runaway. SiC monoliths are exceptional MW and heat conductor scaffolds that absorb and spread the energy to the catalyst powder very effectively. In the PDH with $PtSn/SiO_2$ catalyst, the microfixed bed demonstrated uniform temperatures in the bulk and stable operation (fig. S27) without any arcing even at >700°C. The catalyst loading in the microfixed beds is comparable but lower than that of fixed beds (*16*). However, monoliths and foams have enhanced heat and mass transfer compared to fixed beds and can achieve higher yields to compensate for the lower loading.

Cobenefits from electrification are essential to outweigh the higher cost of modular systems compared to traditional reactors and of electricity. With this in mind, we evaluated CH and MW reactors at comparable conditions to identify these cobenefits while ensuring the same bulk reactor temperature. Critically, we introduced high-temperature measurement capability under MWs to compare reactors and demonstrated identical bulk temperatures and initial performance at lower temperatures.

The processes reveal notable disparities in performance and mechanism (Fig. 7). The CH reactivity above 600°C stems from thermal cracking via gas-phase reactions to methane, C_2 hydrocarbons, and coke precursors, consistent with thermodynamic calculations and catalyst deactivation (*67*), occurring over the entire system due to the unselective furnace heating. Loss of selectivity stems from

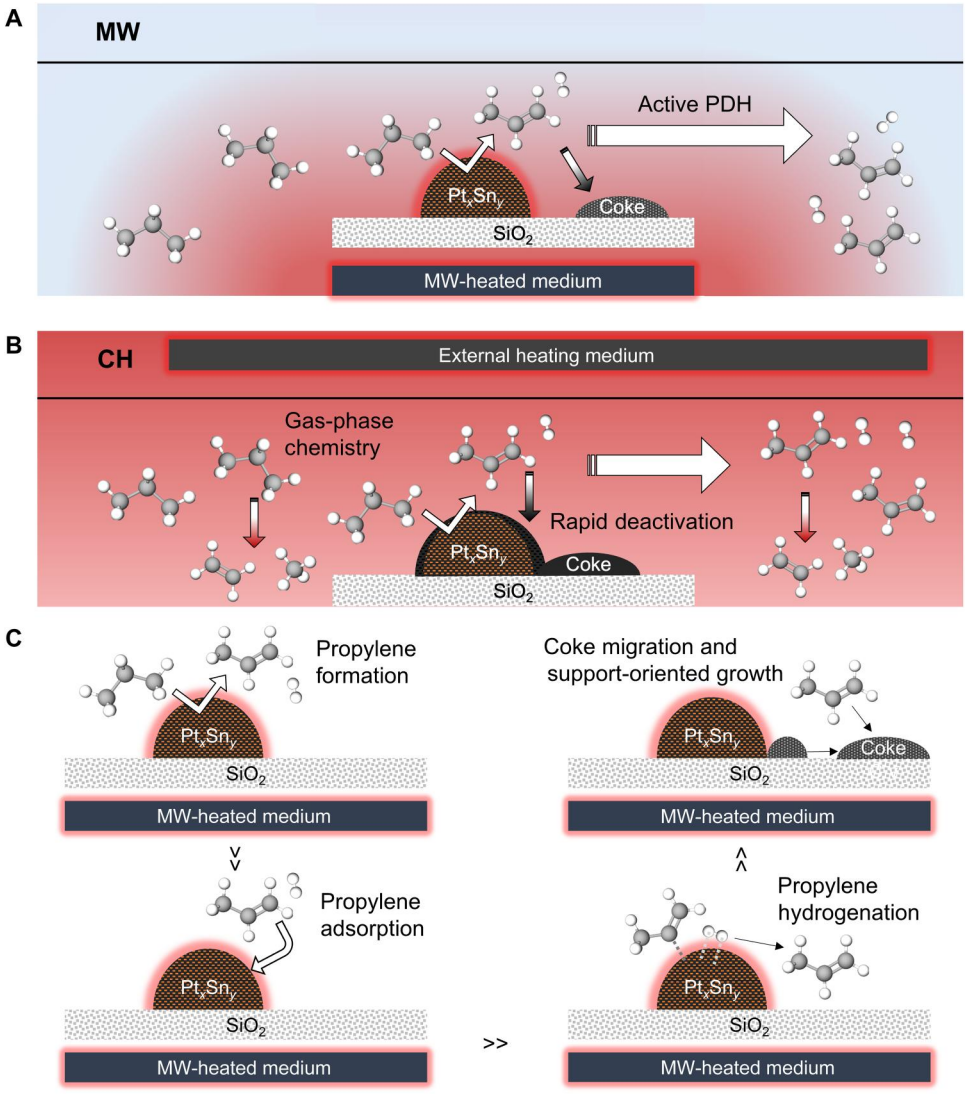

Fig. 7. Schematic illustration of PDH at different heating modes. (**A**) PDH under CH and (**B**) MWs. (**C**) Proposed coke deposition mechanisms under MWs.

gas-phase chemistry rather than unselective paths on the catalyst. It appears that the cracked products enhance catalyst coke formation. Excessive coke forces commercial operations to lower temperatures, giving lower reaction rates and requiring larger reactors and frequent regeneration, reducing productivity, and accelerating the loss of catalytic activity by sintering. Despite being hard, coke is burnt off at lower temperatures catalyzed by the metal nanoparticles (*68*).

The enhanced performance of the MWs is associated with lower power required for heating (fig. S28). CH consumes more power than MW, and LCH500 (55.4 W) and LCH700 (96.0 W) consume comparable power as the MW500 (57.6 W) and MW700 (82.8 W) do when the MW reactor is not insulated. To ensure a fair comparison, the MW reactor should also be insulated. Heat losses depend on the heating mode. A detailed comparison of power consumption will be carried out in future research.

MWs demonstrate higher reactivity and superior selectivity and substantially reduce coke and sintering. MWs are localized in the MW zone and prevent extensive gas-phase chemistry, retaining high selectivity to propylene even at high temperatures (>700°C). The coke precursor formed on the catalyst absorbs MWs and creates a nanoscopic hot spot, leading to their hydrogenation on the metal and desorption or migration to the support. The coke amount is less and more defective. Despite having more defects, it comes off at higher temperatures than CH, an indication that is far away from the metal nanoparticles (*69*) and is burned off noncatalytically. Our data provide strong evidence that the metal nanoparticles focus the electromagnetic field, and microscopic temperature gradients develop, given the poor conductivity of the silica support. These temperature gradients can be rationalized by ballistic rather than the conventional heat transfer conduction mechanism. These temperature gradients can change the coke precursor formation rates, the sintering, and the distribution of metal sites, and thus the fundamental catalyst structure, properties, and chemistry.

Two phenomena may be responsible for the retarded sintering under MWs. First is the adsorbate-induced sintering. Coke

formation involves dehydrogenation and carburization that can instigate metal sintering, leading to agglomeration and loss of active surface area. In MWs, the reduction of coke results in less sintering, preserving the structural integrity of the metal catalyst. Second, the interfacial energy is temperature dependent. In MW irradiation, the colder support reduces the surface energy, effectively quenching nanoparticle growth and coalescence.

MATERIALS AND METHODS

Catalyst, monolith, and quartz beads preparation

The $PtSn/SiO_2$ catalyst was prepared using the incipient wetness impregnation technique. H_2PtCl_6 solution (8 wt %; Sigma-Aldrich) and $SnCl_4$ solution (> 98%; Sigma-Aldrich) were used as Pt and Sn precursors, respectively. The precursors were added to the SiO_2 support (Fuji Silysia Chemical Ltd., G-6; average pore diameter = 6 nm, pore volume = 0.70 ml g^{-1}, surface area = 500 m^2 g^{-1}, calcined at 700°C for 1 hour) to achieve 2 wt % Pt and 1.2 wt % Sn, corresponding to 1:1 atomic ratio. The precursor solution was added and mixed thoroughly until the support was incipiently wet. The impregnated samples were dried at a hotplate and calcined in air at 500°C for 3 hours with a 5°C min^{-1} ramp at 200 SCCM of air. The reduction was then conducted at 600°C for 2 hours with a ramp of 5°C min^{-1}. After reduction, the furnace was cooled down to 100°C, and the gas was switched to an inert atmosphere before being cooled to room temperature (*28*). The catalysts were pelletized and sieved to 40 to 60 mesh size for uniform size. The catalyst was reduced in situ every time before the reaction at 600°C for 30 min with a ramp of 10°C min^{-1}. A 300-CPSI (cells per square inch) SiC monolith was cut from a commercial diesel particle filter (Ibiden, USA) using a sharp blade to have 21 square channels with a unit area of 1.3 mm × 1.3 mm, a wall thickness of 0.18 mm, an area of 9 mm by 9 mm, and a height of 15 mm. To remove any impurities, the monolith was calcined at 700°C for 2 hours with a ramp of 10°C min^{-1} in static air and was ultrasonicated in an acetone solution. Quartz beads of 60 to 80 mesh were prepared from sterilized high-temperature glassware (QSI Quartz; >99.99% SiO_2, working temperatures of ~1300°C) calcined at 700°C for 6 hours with a ramp of 5°C min^{-1} and used to dilute the catalyst and pack the monolith.

MW and conventional reactor setups

The $PtSn/SiO_2$ catalyst (typically 10.0 mg, 0.25 to 0.4 mm) and quartz bead pellets (1050 mg, 0.18 to 0.25 mm) were mixed (total volume = 1.07 ml) and packed over a SiC monolith (1.3 mm by 1.3 mm by 15 mm, 0.35 g, wall thickness = 0.18 mm, volume = 0.11 ml) in a quartz tube (outer diameter = 12 mm, inner diameter = 10 mm) for CH and MW heating (*16*). The pellet size was selected to eliminate mass transfer limitation (*70*), and the total volume of the catalytic bed is 1.07 ml. A porous quartz frit was inserted to diffuse the gaseous molecules and fix the location of the SiC monolith, catalyst, and quartz beads. A monomode cylindrical MW resonator (ITACA Institute, Spain) was used to provide 2.45 GHz of MWs. The external surface temperatures were measured using a pyrometer (Optris CTlaser, USA) and a high-temperature IR camera transparent to quartz (450° to 1800°C; Optris PI 1M, USA). The MW temperature was PID (Proportional–integral–derivative)-controlled using the pyrometer. An FBG (OFSCN, 800°C capillary seamless steel tube, FBG temperature sensor, ceramic-ended, China) measured T_{center} of the catalyst. The FBG tip is directly inserted into the center hole of the monolith, and the FBG location is fixed using donut-holed frits (fig. S29). A commercial electric furnace (Lindberg Blue M, Thermo Fisher Scientific) was used for the CH setup. The LCH reactor was run using a heating tape (DHT051040LD, 13 mm by 1.22 m, 312 W, OMEGALUX) while measuring the electric power consumption using an electricity usage monitor (P4460, P3 International LLC). The LCH is insulated using a basalt fiber-based heat insulation tape (Titanium Exhaust Heat Wrap, LR Technology). The T_{center} of the CH and LCH catalyst bed at the isothermal region was measured using K-type TCs. The effluent was analyzed using gas chromatography (990 Micro GC, Agilent, USA) equipped with multiple column channels (MS5A SS, 10 m by 0.25 mm by 30 μm; BF, RTS, PoraPlot U FS, 10 m by 0.25 mm by 8 μm; BF, Pre-col: CP-PoraBOND Q, 1 m by 0.25 mm by 3 μm) and a mass spectrometer (MS; OmniStar, Pfeiffer Vacuum, USA).

Reaction conditions

For PDH, 5% C_3H_8 in He with a total flow rate of 50.1 SCCM was controlled using mass flow controllers (MFCs; Brooks GF40 Series, USA) with a catalyst weight of 10 mg (equivalent WHSV = 29.5 g_{C3H8} g_{cat}^{-1} $hour^{-1}$, gas hourly space velocity (GHSV) = 322.8 L_{total} g_{cat}^{-1} $hour^{-1}$). The same flow with a catalyst weight of 100 mg was used for near-equilibrium conditions (WHSV = 2.95 g_{C3H8} g_{cat}^{-1} $hour^{-1}$, GHSV = 32.3 L_{total} g_{cat}^{-1} $hour^{-1}$). For high partial pressure tests, 50% C_3H_8 in He with a total flow rate of 50.1 SCCM was flowed to 1.07 ml of catalyst bed with 100 mg of catalyst and quartz beads (equivalent WHSV = 29.5 g_{C3H8} g_{cat}^{-1} $hour^{-1}$, GHSV = 322.8 L_{total} g_{cat}^{-1} $hour^{-1}$). TOS experiments were performed at 500°, 600°, and 700°C for 3 hours. An 800°C tests were performed by the following temperature program: 1 hour at 500°C, 1 hour at 600°C, 30 min at 700°C, and 30 min at 800°C with 10°C min^{-1} ramp. The inlet gas was equilibrated via a bypass line for 5 min and flowed to the reactor. After the reaction, the catalysts were cooled down by purging 100 SCCM of He for 10 min, followed by 10 SCCM of He until reaching room temperature. All experiments were conducted at atmospheric pressure without hydrogen addition unless specified. For noncatalytic temperature-programmed reactions, a catalytic bed was prepared with quartz beads and SiC monolith under the same flow rate (5% C_3H_8 in He, 50.1 SCCM). For ethylene hydrogenation, 4.3% C_2H_4 and 14% H_2 in He (H_2/C_2H_4 = 3.26) with a total volumetric flow of 51.5 SCCM were flowed to the reactor (spent catalyst weight of 10 mg, WHSV = 17 g_{C2H4} g_{cat}^{-1} $hour^{-1}$) at 45°C and 1 bar(a). The inlet gas at specific compositions was equilibrated via a bypass line for 5 min and flowed to the reactor. Conversion, selectivity, and rate calculations are discussed in note S1 (*70*). The regeneration process involves two steps; first, the spent catalysts are regenerated to 5% O_2 in Ar for 1 hour at 600°C, and then they are reduced under 10% H_2 in He for 30 min at 600°C (ramping rate = 10°C min^{-1}).

Catalyst characterization

The morphologies of $PtSn/SiO_2$ catalysts were obtained using TEMs (Talos F200C and JEM-2010F) in a bright field at 200 kV. The catalyst samples were dry deposited on a lacey carbon film on copper grids (Ted Pella Inc., USA). Distinguishable nanoparticles (more than 250) were manually counted using the ImageJ software with multiple images at different random locations at ×240,000 to ×650,000 magnifications. Ex situ Raman spectra were obtained

using a Raman spectrometer (LabRAM HR Evolution, Horiba Scientific, Japan) in 100 to 4000 cm^{-1} and analyzed in the 1000 to 2000 cm^{-1} range. The instrument setup was as follows: acquisition time = 10 s, accumulation for three times, RTD time = 1 s, laser = 532 nm, neutral density filter = 1%, hole size = 200, grating = 600 (500 nm) at the visible range. Multiple spectra (>10 at different regions) were averaged for each sample. Raman spectra were calibrated using a Si wafer with a peak of 520.8 cm^{-1}. A detailed deconvolution procedure is discussed in note S2 (*54*, *59*, *71*). Temperature-programmed oxidation using O_2 (O_2-TPO) was conducted using a CH setup with the MS. H_2O [mass/charge ratio (m/z = 18), CO (m/z = 28), and CO_2 (m/z = 44)] were analyzed. All signals were normalized by the standard Ar signal (m/z = 40) (*72*). After He purge for 1 hour, the temperature was programmed from room temperature to 900°C with a ramp of 10°C min^{-1}, and 60 SCCM 5% O_2 in Ar gas was flowed through the sample using MFC. All lines to the MS were heated to avoid water condensation. The total area of CO_2 effluent was converted to a coke amount, as discussed in note S1. The TGA of spent catalysts was conducted on a thermal gravimetric analyzer (TA Instrument, Discovery TGA). Samples in the platinum pans were heated at a rate of 10°C min^{-1} under 50 SCCM of air from room temperature to 680°C. The first derivatives (DTG) of the TGA curves were numerically calculated. XPS data were collected for pelletized spent catalyst samples over a Cu plate using a Thermo Fisher K-Alpha+ XPS system with an Al-Kα x-ray monochromatic source and processed using Thermo Avantage software. All spectra were calibrated using a single Si^{4+} peak of SiO_2 at 103.5 eV (*73*). Nitrogen adsorption experiments were conducted using a 3Flex surface characterization analyzer (Micromeritics). A Nicolet 8700 Fourier transform IR (FTIR) spectrometer (Thermo Fisher Scientific) equipped with a Harrick high-temperature reaction chamber was used to perform CO-FTIR spectroscopy in DRIFTS mode. The fresh catalyst was reduced in 10% H_2 in He at 600°C for 30 min, cooled down to 100°C, and saturated with CO using a 10% CO in Ar mixture for 5 min. Physisorbed CO was then purged with Ar, and spectra were collected TOS. The CO-DRIFTS–measured fresh catalyst was then reduced in 10% H_2 in He at 600°C to ensure full CO desorption and cooled down to 500°C to undergo PDH under CH. A 50 SCCM of 10% C_3H_8 in Argon was flowed through the cell, conventionally heated at 500°C, for a designated period. After reaction, the cell was cooled down to 100°C, then CO was supplied for 5 min, and spectra were obtained while purging the system.

CFD simulation of MW resonator using COMSOL software

The reactor-filling SiC monolith embedded with catalyst and pellet particles was approximated as a porous medium. The input power remained constant at 120 W at a constant MW frequency, and the input power absorbed by the material was calculated. The convective heat losses were estimated using suitable heat transfer coefficients satisfying the experimental boundary conditions (T_{wall} and T_{center}). The electromagnetic waves, heat transfer, and fluid flow across the reactor were numerically solved. The cross-sectional heat maps and temperature profiles in the axial and radial directions were obtained. The simulation procedure (*74*–*76*) is explained in note S3.

Supplementary Materials

This PDF file includes:

Notes S1 to S3
Figs. S1 to S29
Table S1

REFERENCES AND NOTES

1. S. T. Wismann, J. S. Engbæk, S. B. Vendelbo, F. B. Bendixen, W. L. Eriksen, K. Aasberg-Petersen, C. Frandsen, I. Chorkendorff, P. M. Mortensen, Electrified methane reforming: A compact approach to greener industrial hydrogen production. *Science* **364**, 756–759 (2019).
2. F. Ausfelder, A. Bazzanella, H. VanBrackle, R. Wilde, C. Beckmann, R. Mills, E. Rightor, C. Tam, N. Trudeau, C. Botschek, Technology roadmap energy and GHG reductions in the chemical industry via catalytic processes (International Energy Agency, 2013).
3. Z. J. Schiffer, K. Manthiram, Electrification and Decarbonization of the Chemical Industry. *Joule* **1**, 10–14 (2017).
4. V. Balakotaiah, R. R. Ratnakar, Modular reactors with electrical resistance heating for hydrocarbon cracking and other endothermic reactions. *AIChE J.* **68**, e17542 (2022).
5. D. Zhao, X. Tian, D. E. Doronkin, S. Han, V. A. Kondratenko, J. D. Grunwaldt, A. Perechodjuk, T. H. Vuong, J. Rabeah, R. Eckelt, U. Rodemerck, D. Linke, G. Jiang, H. Jiao, E. V. Kondratenko, In situ formation of ZnOx species for efficient propane dehydrogenation. *Nature* **599**, 234–238 (2021).
6. D. Obermayer, B. Gutmann, C. O. Kappe, Microwave chemistry in silicon carbide reaction vials: Separating thermal from nonthermal effects. *Angew. Chem. Int. Ed.* **48**, 8321–8324 (2009).
7. R. B. Jackson, A. Vengosh, T. H. Darrah, N. R. Warner, A. Down, R. J. Poreda, S. G. Osborn, K. Zhao, J. D. Karr, Increased stray gas abundance in a subset of drinking water wells near Marcellus shale gas extraction. *Proc. Natl. Acad. Sci.* **110**, 11250–11255 (2013).
8. Y. Dai, J. Gu, S. Tian, Y. Wu, J. Chen, F. Li, Y. Du, L. Peng, W. Ding, Y. Yang, γ-Al_2O_3 sheet-stabilized isolate Co^{2+} for catalytic propane dehydrogenation. *J. Catal.* **381**, 482–492 (2020).
9. J. J. Sattler, A. M. Beale, B. M. Weckhuysen, Operando Raman spectroscopy study on the deactivation of Pt/Al_2O_3 and Pt-Sn/Al_2O_3 propane dehydrogenation catalysts. *Phys. Chem. Chem. Phys.* **15**, 12095–12103 (2013).
10. S. Saerens, M. K. Sabbe, V. V. Galvita, E. A. Redekop, M. F. Reyniers, G. B. Marin, The Positive Role of Hydrogen on the Dehydrogenation of Propane on Pt(111). *ACS Catal.* **7**, 7495–7508 (2017).
11. Q. Dong, Y. Yao, S. Cheng, K. Alexopoulos, J. Gao, S. Srinivas, Y. Wang, Y. Pei, C. Zheng, A. H. Brozena, H. Zhao, X. Wang, H. E. Toraman, B. Yang, I. G. Kevrekidis, Y. Ju, D. G. Vlachos, D. Liu, L. Hu, Programmable heating and quenching for efficient thermochemical synthesis. *Nature* **605**, 470–476 (2022).
12. J. M. Serra, J. F. Borrás-Morell, B. García-Baños, M. Balaguer, P. Plaza-González, J. Santos-Blasco, D. Catalán-Martínez, L. Navarrete, J. M. Catalá-Civera, Hydrogen production via microwave-induced water splitting at low temperature. *Nat. Energy* **5**, 910–919 (2020).
13. T. Santos, M. A. Valente, J. Monteiro, J. Sousa, L. C. Costa, Electromagnetic and thermal history during microwave heating. *Appl. Therm. Eng.* **31**, 3255–3261 (2011).
14. M. Baker-Fales, T.-Y. Chen, D. G. Vlachos, Scale-up of microwave-assisted, continuous flow, liquid phase reactors: Application to 5-Hydroxymethylfurfural production. *Chem. Eng. J.* **454**, 139985 (2023).
15. N. Haneishi, S. Tsubaki, E. Abe, M. M. Maitani, E.-I. Suzuki, S. Fujii, J. Fukushima, H. Takizawa, Y. Wada, Enhancement of Fixed-bed Flow Reactions under Microwave Irradiation by Local Heating at the Vicinal Contact Points of Catalyst Particles. *Sci. Rep.* **9**, 222 (2019).
16. W. Chen, A. Malhotra, K. Yu, W. Zheng, P. J. Plaza-Gonzalez, J. M. Catala-Civera, J. Santamaria, D. G. Vlachos, Intensified microwave-assisted heterogeneous catalytic reactors for sustainable chemical manufacturing. *Chem. Eng. J.* **420**, 130476–130476 (2021).
17. I. Julian, H. Ramirez, J. L. Hueso, R. Mallada, J. Santamaria, Non-oxidative methane conversion in microwave-assisted structured reactors. *Chem. Eng. J.* **377**, 119764 (2019).
18. A. Malhotra, W. Chen, H. Goyal, P. J. Plaza-Gonzalez, I. Julian, J. M. Catala-Civera, D. G. Vlachos, Temperature Homogeneity under Selective and Localized Microwave Heating in Structured Flow Reactors. *Ind. Eng. Chem. Res.* **60**, 6835–6847 (2021).
19. H. Goyal, A. Mehdad, R. F. Lobo, G. D. Stefanidis, D. G. Vlachos, Scaleup of a Single-Mode Microwave Reactor. *Ind. Eng. Chem. Res.* **59**, 2516–2523 (2020).
20. N. Parmar, C. A. Kavale, H. Goyal, A Computationally Fast Method to Simulate Microwave-Heated Monoliths. *Ind. Eng. Chem. Res.* **62**, 2561–2572 (2023).
21. C. O. Kappe, How to measure reaction temperature in microwave-heated transformations. *Chem. Soc. Rev.* **42**, 4977–4990 (2013).

22. A. Ramirez, J. L. Hueso, R. Mallada, J. Santamaria, Microwave-activated structured reactors to maximize propylene selectivity in the oxidative dehydrogenation of propane. *Chem. Eng. J.* **393**, 124746–124746 (2020).
23. S. Alayoglu, C. Aliaga, C. Sprung, G. A. Somorjai, Size and Shape Dependence on Pt Nanoparticles for the Methylcyclopentane/Hydrogen Ring Opening/Ring Enlargement Reaction. *Catal. Lett.* **141**, 914–924 (2011).
24. J. Sa´nchez, N. Segovia, A. Moronta, A. Arteaga, G. Arteaga, E. Choren, Catalyst characterization by a probe reaction: Effect of tin addition in $PtSn/Al_2O_3$. *Appl. Catal. Gen.* **101**, 199–206 (1993).
25. A. Moscu, Y. Schuurman, L. Veyre, C. Thieuleux, F. Meunier, Direct evidence by in situ IR CO monitoring of the formation and the surface segregation of a Pt–Sn alloy. *Chem. Commun.* **50**, 8590–8592 (2014).
26. H. N. Pham, J. J. H. B. Sattler, B. M. Weckhuysen, A. K. Datye, Role of Sn in the Regeneration of $Pt/\gamma\text{-}Al_2O_3$ Light Alkane Dehydrogenation Catalysts. *ACS Catal.* **6**, 2257–2264 (2016).
27. M.-L. Yang, Y.-A. Zhu, X.-G. Zhou, Z.-J. Sui, D. Chen, First-Principles Calculations of Propane Dehydrogenation over PtSn Catalysts. *ACS Catal.* **2**, 1247–1258 (2012).
28. A. H. Motagamwala, R. Almallahi, J. Wortman, V. O. Igenegbai, S. Linic, Stable and selective catalysts for propane dehydrogenation operating at thermodynamic limit. *Science* **373**, 217–222 (2021).
29. Y.-L. Shan, T. Wang, Z.-J. Sui, Y.-A. Zhu, X.-G. Zhou, Hierarchical $MgAl_2O_4$ supported Pt-Sn as a highly thermostable catalyst for propane dehydrogenation. *Catal. Commun.* **84**, 85–88 (2016).
30. Y. Zhang, Y. Zhou, J. Shi, S. Zhou, X. Sheng, Z. Zhang, S. Xiang, Comparative study of bimetallic Pt-Sn catalysts supported on different supports for propane dehydrogenation. *J. Mol. Catal. A Chem.* **381**, 138–147 (2014).
31. C. Sun, J. Luo, M. Cao, P. Zheng, G. Li, J. Bu, Z. Cao, S. Chen, X. Xie, A comparative study on different regeneration processes of $Pt\text{-}Sn/\gamma\text{-}Al_2O_3$ catalysts for propane dehydrogenation. *J. Energy Chem.* **27**, 311–318 (2018).
32. O. B. Belskaya, L. N. Stepanova, T. I. Gulyaeva, S. B. Erenburg, S. V. Trubina, K. Kvashnina, A. I. Nizovskii, A. V. Kalinkin, V. I. Zaikovskii, V. I. Bukhtiyarov, V. A. Likholobov, Zinc influence on the formation and properties of Pt/Mg(Zn)AlO catalysts synthesized from layered hydroxides. *J. Catal.* **341**, 13–23 (2016).
33. T. Wang, F. Jiang, G. Liu, L. Zeng, J. Gong, Effects of Ga doping on $Pt/CeO_2\text{-}Al_2O_3$ catalysts for propane dehydrogenation. *AIChE J.* **62**, 4365–4376 (2016).
34. P. Wang, J. Yao, Q. Jiang, X. Gao, D. Lin, H. Yang, L. Wu, Y. Tang, L. Tan, Stabilizing the isolated Pt sites on $PtGa/Al_2O_3$ catalyst via silica coating layers for propane dehydrogenation at low temperature. *Appl. Catal. Environ.* **300**, 120731 (2022).
35. X. Gao, W. Xu, X. Li, J. Cen, Y. Xu, L. Lin, S. Yao, Non-oxidative dehydrogenation of propane to propene over $Pt\text{-}Sn/Al_2O_3$ catalysts: Identification of the nature of active site. *Chem. Eng. J.* **443**, 136393 (2022).
36. R. Ryoo, J. Kim, C. Jo, S. W. Han, J.-C. Kim, H. Park, J. Han, H. S. Shin, J. W. Shin, Rare-earth–platinum alloy nanoparticles in mesoporous zeolite for catalysis. *Nature* **585**, 221–224 (2020).
37. L. Shi, G.-M. Deng, W.-C. Li, S. Miao, Q.-N. Wang, W.-P. Zhang, A.-H. Lu, Al_2O_3 Nanosheets Rich in Pentacoordinate Al^{3+} Ions Stabilize Pt-Sn Clusters for Propane Dehydrogenation. *Angew. Chem. Int. Ed.* **54**, 13994–13998 (2015).
38. M.-H. Lee, B. M. Nagaraja, P. Natarajan, N. T. Truong, K. Y. Lee, S. Yoon, K.-D. Jung, Effect of potassium addition on bimetallic $PtSn/\theta\text{-}Al_2O_3$ catalyst for dehydrogenation of propane to propylene. *Res. Chem. Intermed.* **42**, 123–140 (2016).
39. N. V. Srinath, A. Longo, H. Poelman, R. K. Ramachandran, J.-Y. Feng, J. Dendooven, M.-F. Reyniers, V. V. Galvita, In Situ XAS/SAXS Study of Al_2O_3-Coated PtGa Catalysts for Propane Dehydrogenation. *ACS Catal.* **11**, 11320–11335 (2021).
40. Z. Xu, R. Xu, Y. Yue, P. Yuan, X. Bao, E. Abou-Hamad, J.-M. Basset, H. Zhu, Bimetallic Pt-Sn nanocluster from the hydrogenolysis of a well-defined surface compound consisting of [(AlO)Pt(COD)Me] and [(AlO)$SnPh_3$] fragments for propane dehydrogenation. *J. Catal.* **374**, 391–400 (2019).
41. T. Srisakwattana, S. Watmanee, S. Wannakao, C. Saiyasombat, P. Praserthdam, J. Panpranot, Comparative incorporation of Sn and In in Mg(Al)O for the enhanced stability of Pt/MgAl(X)O catalysts in propane dehydrogenation. *Appl. Catal. Gen.* **615**, 118053 (2021).
42. L.-L. Shen, K. Xia, W.-Z. Lang, L.-F. Chu, X. Yan, Y.-J. Guo, The effects of calcination temperature of support on PtIn/Mg(Al)O catalysts for propane dehydrogenation reaction. *Chem. Eng. J.* **324**, 336–346 (2017).
43. G.-Q. Ren, G.-X. Pei, Y.-J. Ren, K.-P. Liu, Z.-Q. Chen, J.-Y. Yang, Y. Su, X.-Y. Liu, W.-Z. Li, T. Zhang, Effect of group IB metals on the dehydrogenation of propane to propylene over anti-sintering $Pt/MgAl_2O_4$. *J. Catal.* **366**, 115–126 (2018).
44. Y. Nakaya, F. Xing, H. Ham, K. I. Shimizu, S. Furukawa, Doubly Decorated Platinum-Gallium Intermetallics as Stable Catalysts for Propane Dehydrogenation. *Angew. Chem. Int. Ed. Engl.* **60**, 19715–19719 (2021).
45. T. Cao, X. Dai, F. Li, W. Liu, Y. Bai, Y. Fu, W. Qi, Efficient non-precious metal catalyst for propane dehydrogenation: Atomically dispersed cobalt-nitrogen compounds on carbon nanotubes. *ChemCatChem* **13**, 3067–3073 (2021).
46. N. Kaylor, R. J. Davis, Propane dehydrogenation over supported Pt-Sn nanoparticles. *J. Catal.* **367**, 181–193 (2018).
47. Z. Han, S. Li, F. Jiang, T. Wang, X. Ma, J. Gong, Propane dehydrogenation over Pt-Cu bimetallic catalysts: The nature of coke deposition and the role of copper. *Nanoscale* **6**, 10000–10008 (2014).
48. T. W. Hansen, A. T. DeLaRiva, S. R. Challa, A. K. Datye, Sintering of catalytic nanoparticles: Particle migration or Ostwald ripening? *Acc. Chem. Res.* **46**, 1720–1730 (2013).
49. A. Malhotra, M. Maldovan, Surface scattering controlled heat conduction in semiconductor thin films. *J. Appl. Phys.* **120**, (2016).
50. M. Larsson, M. Hultén, E. A. Blekkan, B. Andersson, The effect of reaction conditions and time on stream on the coke formed during propane dehydrogenation. *J. Catal.* **164**, 44–53 (1996).
51. S. Sokolov, M. Stoyanova, U. Rodemerck, D. Linke, E. V. Kondratenko, Comparative study of propane dehydrogenation over V-, Cr-, and Pt-based catalysts: Time on-stream behavior and origins of deactivation. *J. Catal.* **293**, 67–75 (2012).
52. Q. Li, Z. Sui, X. Zhou, Y. Zhu, J. Zhou, D. Chen, Coke formation on $Pt\text{–}Sn/Al_2O_3$ catalyst in propane dehydrogenation: coke characterization and kinetic study. *Top. Catal.* **54**, 888–896 (2011).
53. A. Iglesias-Juez, A. M. Beale, K. Maaijen, T. C. Weng, P. Glatzel, B. M. Weckhuysen, A combined in situ time-resolved UV–Vis, Raman and high-energy resolution x-ray absorption spectroscopy study on the deactivation behavior of Pt and PtSn propane dehydrogenation catalysts under industrial reaction conditions. *J. Catal.* **276**, 268–279 (2010).
54. J. Xu, Q. He, Z. Xiong, Y. Yu, S. Zhang, X. Hu, L. Jiang, S. Su, S. Hu, Y. Wang, J. Xiang, Raman spectroscopy as a versatile tool for investigating thermochemical processing of coal, biomass, and wastes: Recent advances and future perspectives. *Energy Fuel* **35**, 2870–2913 (2021).
55. Z. Wang, Y. Chen, S. Mao, K. Wu, K. Zhang, Q. Li, Y. Wang, Chemical insight into the structure and formation of coke on PtSn alloy during propane dehydrogenation. *Adv. Sustain. Syst.* **4**, 2000092 (2020).
56. W. Lin, K.-S. Moon, S. Zhang, Y. Ding, J. Shang, M. Chen, C.-P. Wong, Microwave Makes Carbon Nanotubes Less Defective. *ACS Nano* **4**, 1716–1722 (2010).
57. S. Chen, X. Chang, G. Sun, T. Zhang, Y. Xu, Y. Wang, C. Pei, J. Gong, Propane dehydrogenation: Catalyst development, new chemistry, and emerging technologies. *Chem. Soc. Rev.* **50**, 3315–3354 (2021).
58. V. Sharma, D. Uy, A. Gangopadhyay, A. O'Neill, W. A. Paxton, A. Sammut, M. A. Ford, P. B. Aswath, Structure and chemistry of crankcase and exhaust soot extracted from diesel engines. *Carbon* **103**, 327–338 (2016).
59. C. C. Zhang, S. Hartlaub, I. Petrovic, B. Yilmaz, Raman spectroscopy characterization of amorphous coke generated in industrial processes. *ACS Omega* **7**, 2565–2570 (2022).
60. D. H. McNeil, H. G. Schulze, E. Matys, T. Bosak, Raman spectroscopic analysis of carbonaceous matter and silica in the test walls of recent and fossil agglutinated foraminifera. *AAPG Bulletin* **99**, 1081–1097 (2015).
61. J. Cunha, T. L. Guo, G. Della Valle, A. N. Koya, R. Proietti Zaccaria, A. Alabastri, Controlling light, heat, and vibrations in plasmonics and *Phononics*. *Opt. Mater.* **8**, 2001225 (2020).
62. T. Ano, S. Tsubaki, A. Liu, M. Matsuhisa, S. Fujii, K. Motokura, W.-J. Chun, Y. Wada, Probing the temperature of supported platinum nanoparticles under microwave irradiation by in situ and operando XAFS. *Commun. Chem.* **3**, 86 (2020).
63. S. Tsubaki, T. Matsuzawa, T. Higuchi, S. Fujii, Y. Wada, Determining the influence of microwave-induced thermal unevenness on vanadium oxide catalyst particles. *Chem. Eng. J.* **433**, 133603 (2022).
64. J. Vicente, C. Montero, J. Ereña, M. J. Azkoiti, J. Bilbao, A. G. Gayubo, Coke deactivation of Ni and Co catalysts in ethanol steam reforming at mild temperatures in a fluidized bed reactor. *Int. J. Hydrogen Energy* **39**, 12586–12596 (2014).
65. B. Robinson, A. Caiola, X. Bai, V. Abdelsayed, D. Shekhawat, J. Hu, Catalytic direct conversion of ethane to value-added chemicals under microwave irradiation. *Catal. Today* **356**, 3–10 (2020).
66. Y. Deng, X. Bai, V. Abdelsayed, D. Shekhawat, P. D. Muley, S. Karpe, C. Mevawala, D. Bhattacharyya, B. Robinson, A. Caiola, J. B. Powell, A. P. van Bavel, J. Hu, G. Veser, Microwave-assisted conversion of methane over H-(Fe)-ZSM-5: Evidence for formation of hot metal sites. *Chem. Eng. J.* **420**, 129670 (2021).
67. Z. Lian, C. Si, F. Jan, S. Zhi, B. Li, Coke deposition on Pt-based catalysts in propane direct dehydrogenation: Kinetics, suppression, and elimination. *ACS Catal.* **11**, 9279–9292 (2021).
68. L. Liwu, Z. Tao, Z. Jingling, X. Zhusheng, Dynamic process of carbon deposition on Pt and Pt–Sn catalysts for alkane dehydrogenation. *Appl. Catal.* **67**, 11–23 (1990).

69. B. K. Vu, M. B. Song, I. Y. Ahn, Y. W. Suh, D. J. Suh, W. I. Kim, H. L. Koh, Y. G. Choi, E. W. Shin, Propane dehydrogenation over Pt-Sn/Rare-earth-doped Al_2O_3: Influence of La, Ce, or y on the formation and stability of Pt-Sn alloys. *Catal. Today* **164**, 214–220 (2011).
70. M. Sheintuch, O. Liron, A. Ricca, V. Palma, Propane dehydrogenation kinetics on supported Pt catalyst. *Appl. Catal. Gen.* **516**, 17–29 (2016).
71. A. Sadezky, H. Muckenhuber, H. Grothe, R. Niessner, U. Pöschl, Raman microspectroscopy of soot and related carbonaceous materials: Spectral analysis and structural information. *Carbon* **43**, 1731–1742 (2005).
72. B. J. Adelman, T. Beutel, G. D. Lei, W. M. H. Sachtler, Mechanistic cause of hydrocarbon specificity over Cu/ZSM-5 and Co/ZSM-5 catalysts in the selective catalytic reduction of NOx. *J. Catal.* **158**, 327–335 (1996).
73. N. Koshizaki, H. Umehara, T. Oyama, XPS characterization and optical properties of Si/SiO_2, Si/Al_2O_3 and Si/MgO co-sputtered films. *Thin Solid Films* **325**, 130–136 (1998).
74. H. Goyal, D. G. Vlachos, Multiscale modeling of microwave-heated multiphase systems. *Chem. Eng. J.* **397**, 125262 (2020).
75. H. Goyal, S. Sadula, D. G. Vlachos, Microwave heating of slurries. *Chem. Eng. J.* **417**, 127892 (2021).
76. S. Whitaker, The Method of Volume Averaging in *Theory and applications of transport in porous media*, Springer Science & Business Media (vol. 13, 1998).

Acknowledgments

Funding: The initial part of this work was supported by the Department of Energy (DOE)'s Office of Energy Efficient and Renewable Energy's Advanced Manufacturing Office under award number DE-EE0007888-8.3. The latter part was supported by the US DOE award number DE-SC0024085. The Delaware Energy Institute gratefully acknowledges the support and partnership of the State of Delaware toward the RAPID (Rapid Advancement in Process Intensification Deployment) projects. **Author contributions:** Conceptualization: Y.K., W.Z., and D.G.V. Methodology: Y.K., C.W., W.Z., H.G., and D.G.V. Investigation: Y.K., C.A.K., K.Y., and E.S. Visualization: Y.K. Supervision: W.Z., H.G., and D.G.V. Resources: C.W., K.Y., R.M., J.S., and J.M.C.-C. Validation: R.M., I.J., and J.M.C.-C. Writing—original draft: Y.K. and D.G.V. Writing—review and editing: Y.K., I.J., J.S., W.Z., and D.G.V. Project administration and funding acquisition: D.G.V. **Competing interests:** The authors declare that they have no competing interests. **Data and materials availability:** All data needed to evaluate the conclusions in the paper are present in the paper and/or the Supplementary Materials.

Submitted 19 May 2023
Accepted 15 August 2023
Published 15 September 2023
10.1126/sciadv.adi8219